공학 석사 학위논문

Development and Fundamental Study of Neutron Target System by 100 MeV Pulsed Proton Beam

100 MeV 양성자 펄스 빔을 이용한 중성자 표적 시스템 개발 및 전산모사 연구

2020 년 7 월

서울대학교 대학원

에너지시스템공학부

임 수 빈

Development and Fundamental Study of Neutron Target System by 100 MeV Pulsed Proton Beam

지도교수 황 용 석

이 논문을 공학석사 학위논문으로 제출함

2020 년 7 월

서울대학교 대학원

에너지시스템공학부

임 수 빈

임수빈의 공학석사 학위논문을 인준함

2020 년 7 월

위 원 장	김 은 희	(인)
부위원장	황 용 석	(인)
위 원	정 경 재	(인)

Abstract

Development and Fundamental Study of Neutron Target System by 100 MeV Pulsed Proton Beam

Soobin Lim

Department of Energy Systems Engineering

The Graduate School

Seoul National University

A broad research regarding 100 MeV neutron target and its detection system is described in this thesis. The goal of this research is to develop a fast neutron target which can imitate atmospheric neutron for soft error assessment in microelectronic devices. Primary measurement on fast neutron with a Cu beam dump irradiated by 100 MeV protons is conducted and processed. Then, a design and brief measurement on gamma flash type neutron Time-Of-Flight (TOF) system is conducted to develop a spectroscopy system for detection of fast neutron from range of 10 to 100 MeV. Both measurement successfully measured neutron fluxes and neutron energy generated from Cu beam dump, and verification on the measurement setup is verified with Geant4 Monte-Carlo code. Finally, a new design on fast neutron target which can take

thermal deposition up to 2 Kw is carried out and evaluated with a simulation. The target is expected to deliver atmospheric-like fast neutron with a suitable flux to an irradiation station located 5 m, 7º away from the target.

Contents

List of Figures

Chapter 1. Introduction

There is an increasing demand in neutron sources in both science and industrial areas due to increasing studies of neutrons for applications to those areas, but there are not many available neutron source facilities adequate for such purposes. Especially, over decades, frequent activities were related to semiconductors of neutrons originated by cosmic rays. Energetic particles from space pass through and interact with air layers on the Earth, causing a cascade of neutrons from fast to thermal neutrons. IBM and other electronic industries [1,2] found that the terrestrial cosmic-ray neutrons cause the soft errors of semiconductors inside sensitive electronics, and the reactions causing soft errors are dependent on neutron energy [3–6]. Thus, to comprehensively understand the effects of neutrons on electronics, it is essential to examine the electronic device with different ranges of neutron energy. Therefore, the Korea Multi-Purpose Accelerator Complex (KOMAC) that is affiliated to the Korea Atomic Energy Research Institute (KAERI) is to provide a neutron source resembling the fast neutrons from 1 MeV to 100 MeV of the terrestrial neutron spectrum, using a 100 MeV pulsed proton linear accelerator.

In this thesis, a thorough review on 100 MeV atmospheric-like neutron generation system is described, from a fundamental study of neutron generation to fast neutron measurement system. The properties of neutron generation by target geometry and materials are studied to determine the most suitable material and configuration for generating neutron spectrum similar to neutrons caused by cosmic ray bombarded down to ground level. It is revealed that the fast neutrons are generated mostly on the backside of the target with respect to face plate of proton irradiation, and the thickness of target should be optimized in order to maximize fast neutron generation at the back plate. Studies on stopping power and neutron generation is followed for the optimization on target thickness. To achieve the maximum fast neutron generation and neutron yield per proton irradiation, the 100 MeV proton must be depositing most of its energy inside of the target while keeping the thickness minimized.

Studies on neutron transport and neutron detection is also accompanied to comprehensively understand the process of neutron measurement and verification of neutron simulation. Environments and structures of the neutron detection circumstances are implemented in the simulation to properly estimate effects by structures in the site and concrete walls enclosing the irradiation station. The simulation is conducted altogether with neutron generation, transport, and detector response, so that the whole process can be included in single simulation to enable a direct comparison with actual measurement with the same configuration.

Then, preliminary neutron generation experiment is carried with copper beam dump previously installed at the end of the accelerator. By removing borated water and cooling water inside the beam dump, the copper dump can be utilized as a primitive neutron target. Proton beam is irradiated to the dump with 0.5 kW average power and 5 uA average current, and 1” cylindrical stilbene crystal coupled with Hamamatsu h11934-100 photomultiplier tube (PMT) is used as a neutron detector. Signals obtained from the experiment is processed with pulse shape discrimination (PSD) method to distinguish neutron signals from gamma signals. The neutron signals are drawn to a histogram, and compared with a simulation conducted with the same configuration. The result shows rough agreement on both spectra and neutron countrate on the detector.

Finally, we designed a water-cooled solid target suitable to produce fast neutrons with a similar energy spectrum than the cosmic-ray-induced ground-level neutron spectrum, based on the studied conducted above. The beam power loading on the target is assumed at 2 kW when considering the nominal operation of the 100 MeV proton accelerator at KOMAC. Neutron yield and energy spectrum are calculated using the Geant4 Monte-Carlo simulation toolkit for various candidate materials and configurations and compared with the atmospheric neutron spectrum in New York [1,2]. ANSYS Fluent is used to assess the thermal integrity of the target when it is irradiated by the proton beam at its desired performance. The cooling channel is placed directly behind the target to stop the moderated protons at the target at the water to prevent the target from hydrogen blistering on the inside. With the designed target

assembly, we also conduct a comprehensive simulation to evaluate the neutron fluence and acceleration factor expected at the irradiation station at 5 m and 7° away from the target.

Furthermore, conceptual design on atmospheric-like neutron target is conducted. Because neutron generation properties are slightly different by materials, the properties are parametrized and modeled as a function of energy by a unit thickness, so that a mixture of metals can generate more atmospheric-like neutron target materials than pure metallic targets. As a result, similarity parameter of neutron spectrum for the mixture material exhibits greater performance then previously selected materials. This particular methodology can be applied in designing a target for the future accelerator upgrade to 200 MeV, where the similarity of spectra between generated neutrons and atmospheric neutron becomes more critical.

1.1. Spallation Neutrons.

Spallation neutron source has been one of the most commonplace source of fast neutrons since the discovery of spallation reaction in 1947 [7]. When charged particles with sufficiently high energy (usually above 100 MeV) is irradiated to material elements with massive nucleons, spallation reaction takes place to generate multiple fragments of smaller mass of nuclei with neutrons. As a result, a cascade of various particles “spalled” from the irradiated particles, so that large amount of gamma rays, neutrons, and other particles are generated and escape outside of the target. This particular method has been widely used with fast proton accelerators up to 1 GeV [8], due to highly efficient energy to neutron conversion ratio [7]. Facilities with accelerated proton energy up to 1 GeV has been operating since few decades ago, and spallation properties at that energy range has been verified with both simulation and experiment over time. However, energy ranges at 100 MeV proton is a commonly known as a border line for spallation reaction to occur, and it is rarely studied in respect of its properties in neutron generation behavior. Therefore, the goal of this thesis is to build a neutron generating target for 100 MeV proton beam from a fundamental research for spallation properties at 100 MeV.

1.2. Atmospheric Neutrons.

Atmospheric neutrons are generated from galactic cosmic ray interacting with particles in the atmosphere. Energetic particles from the cosmic ray collides with nuclei in the air to generate secondary particles including high energy neutrons [1]. Energy of the neutrons can be as high as GeV, and the neutron fluence reaches down to sea level. The neutron fluence and energy measured at sea level in New York City by Gordon et al, is used as the most commonly used reference of ground level data for evaluation on effects by neutrons to electrical devices [9].

According to the research, fluence of the neutron from 1 MeV to above is approximately 20 n / cm^2hr, and the differential flux d $\phi_0(E)/dE$ can be described as following:

$$\frac{d\phi_0(E)}{dE} = \sum_{j=1}^{2} c_j \exp[-\beta_j(\ln(E))^2 + \gamma_j \ln(E)] \quad (1.1)$$

The values of the parameters c_j, β_j, and γ_j are given as [1]:

Table 1. Fitted Parameters for Analytic Differential Neutron Fluence.

FITTED PARAMETERS FOR THE ANALYTIC MODEL

j	β_j	γ_j	c_j
1	0.3500	2.1451	1.006×10^{-6}
2	0.4106	-0.6670	1.011×10^{-3}

The presence of atmospheric neutron has raised attention to industry in electrical devices due to an importance of soft errors with advanced microelectronics with sizes less than 100 nm, where the devices become more sensitive to charges induced by fast neutrons interacting with silicon, boron, and other elements inside it [6, 10, 12]. When atmospheric neutron collides with sensitive part of microelectronics, the interaction induces charges that are sufficient to change its state of register in the electronics, causing nondestructive bit-flip error in the end. Such incidents can be caused by variety of processes; The so-called Single Event Effects includes Single Event Upset (SEU), Single Event Latchup (SEL), and Single Event Burnout (SEB) [10]. Especially,

SEU is induced from broad range of fast neutron energies starting from 1 MeV [6]. Facilities providing broad range of neutrons with high fluxes with spallation reactions and nuclear reactions has been utilized to imitate atmospheric neutrons and estimate SEE rate with significantly higher flux of neutrons, so-called accelerated testing. The fluence over a certain amount of time compared to that of atmospheric neutron is defined as an acceleration factor. The relationship between neutron SEE and accelerated testing is formulated by JEDEC as following [9,11]:

$$\mathrm{A} = \int_{E_{min}}^{\infty} \frac{\emptyset_{acc}(E)dE}{\emptyset_{atm}(E)dE} \quad (1.2)$$

The soft error rate is evaluated as below [IEEE]:

$$\mathrm{R} = \int_{E_{min}}^{\infty} \sigma(E)\emptyset_{acc}(E)dE \quad (1.3)$$

Where soft error cross section $\sigma(\mathrm{E})$ is defined as :

$$\sigma(E) = \frac{\text{Number of soft error events}}{\emptyset_{acc} * Time} \quad (1.4)$$

However, in experimental situation, it is difficult to obtain soft error cross section function with differential energy due to continuous spectrum shape of neutrons and lack of monoenergetic neutron sources at this high energy. Therefore, acceleration factor A and soft error R cannot be fully considered with different type of reactions and different neutron energy. When a spallation neutron draws greatly different neutron spectrum compared with that of atmospheric neutrons, acceleration factor cannot represent an accelerated soft error rate due to soft error cross section at different energies. Most facilities which provides white neutron sources with spallation reaction is not designed in consideration of similarity with atmospheric neutron spectrum, and therefore there would be a disparity between soft error rate obtained by an accelerated testing and actual soft error. At this point where demand of atmospheric-like neutron providing facilities is increasing, some of such facilities has been developed or is in construction, but it is still insufficient to satisfy the demand from industrial and science area for this specific purpose.

The ultimate goal of this research is to build a fast neutron target above 1 MeV in consideration of similarity with atmospheric neutron spectrum with sufficient

neutron flux for accelerated soft error testing. Moreover, development of fast neutron detection technique is accompanied for further verification of built neutron target in the future to provide a reliable soft error assessment for neutron users.

1.3. Neutron Detection.

To correctly demonstrate performance of a designed neutron target, characterization of target generated neutron via experimental neutron detection is required. Development for neutron detection method and system construction is accompanied along with design of the target. Characterization of the neutron target should include neutron spectrum and flux measurement to obtain required information to properly evaluate an accelerated test for electronic devices. Therefore, though it had to be put off to a future assignment to evaluate actual designed target performance due to a matter of time, development for such method and system assembly is carried on as a preparation. In this research, prototype fast neutron measurement system and preliminary flux measurement is arranged.

Throughout this research, neutron detection with scintillation crystal coupled with photomultiplier tube (PMT) is utilized. Fast neutron detection with an organic scintillator and energy measurement with neutron Time-of-Flight (TOF) method is applied. Organic scintillators possess several advantageous properties for fast neutron detections by its ability to perform pulse shape discrimination (PSD) to separate neutron signals from gamma signals, relatively less sensitivity to gamma particles, and fast signal decay time [13]. Detail description on fast neutron measurement implemented for this research is discussed in later part of the paper.

Chapter 2. Experimental Setup

2.1. Neutron Production.

2.1.1. 100 MeV Proton Linear Accelerator.

Source of the fast neutron target is provided by a 100 MeV proton linear accelerator operated in KOrea Multi-Purpose Accelerator Complex (KOMAC), affiliated with Korea Atomic Energy Research Institute (KAERI) in Gyoungju, South Korea. The linear accelerator delivers high energy proton at maximum energy of 100 MeV with average power of 1 kW. Maximum repetition rate for 10 Hz at average beam current of 10 uA [14]. Pulse width of proton beam is available from 20 us to 500 us with three available beam lines including one low-current irradiation station. In the facility, there is a rise of demand of fast neutron source from various types of users, promoting importance of this research. Fig 2.1 illustrates an simplified overview of 100 MeV proton linear accelerator.

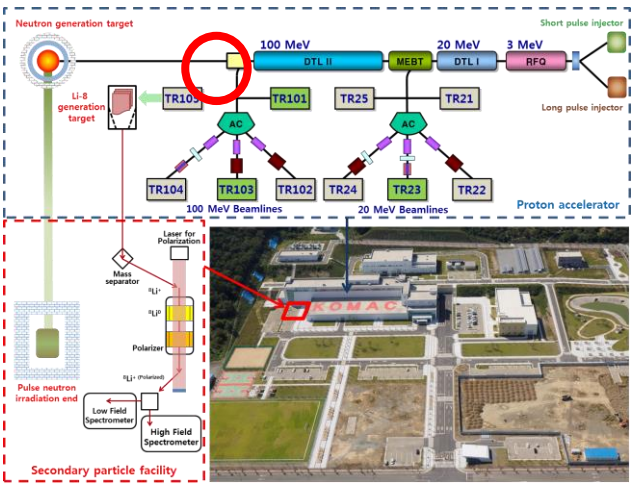

Figure 2.1 Overview of 100 MeV linear accelerator in KOMAC, KAERI

2.1.2. Proton Beam Dump.

There is a beam dump at the end of accelerator before a bending magnet which directs protons to individual beam lines as indicated by red circle in Fig 2.1. Prior to installation of the neutron target, the beam dump is utilized as a primitive neutron target. The beam dump consists of beam chamber which surrounds the whole structure, a beam dump cone, and a jacket for it. Dump cone consists of oxygen-free copper, and others consist with stainless steel. It is directly connected with the beam line with 8" CF flange, keeping the vacuum of dump cone lower than 10^7 torr. The other side of the dump chamber is filled with cooling water and borated water to stabilize the dump temperature and suppress unwanted neutron radiation. Fig 2.2 shows a diagram of beam chamber. Jacket part is connected with external water pump to provide cooling water, and rest of the dump chamber is filled borated water for a normal operation. For this particular case, both of the water is removed so that generated neutrons from beam dump is not intervened by the water layers. Irradiated part of the dump cone is sufficiently thick to fully stop 100 MeV proton inside of its medium. By sending 100 MeV proton beam into the dump without surrounding water, dump cone serves as a thick copper target, emitting fast neutrons outside of the chamber.

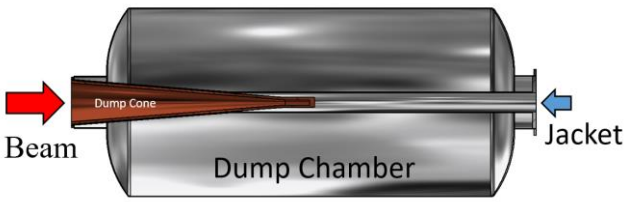

Figure 2.2 Structure of beam dump.

2.2. Fast Neutron Measurement.

2.2.1 Radiation Detection Instruments

Neutron detection system prepared for this experiment consists radiation detectors, PMTs, and a MCA for DAQ. Important components are mentioned in the list below.

Scintillation detector:

1. 1” cylindrical Stilbene crystal
2. 1” cylindrical LaBr3:Ce crystal

PMTs:

1. Hamamatsu H11934-100
2. Hamamatsu R1924A tube with E2924 PM base

MCA:

1. Caen DT5751 digitizer
2. Caen N6725 digitizer

The system comprises three main components listed above with a high voltage supply to apply bias voltage to PMTs and a PC to receive data from MCA. A detection system is illustrated below in Fig. 2.3 [15].

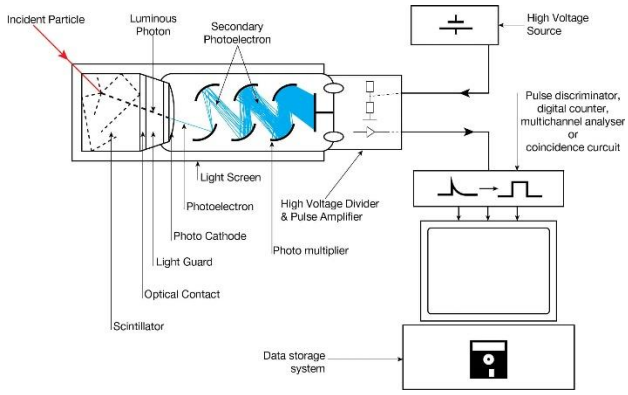

Figure 2.3. A typical diagram of radiation detection system using scintillator.

When an energetic particle with electric charge interacts with mediums inside the scintillation detector, electrons surrounding the scintillator molecule is excited and transferred to lower state, emitting a scintillating photon. Photons converted from deposited energy of charged particle is collected by a photocathode of PMT window, and the photocathode puts out photoelectrons proportional to its characteristic quantum efficiency. The electrons are amplified by dynode structures inside a PMT to produce a detectable pulse signal. The pulse signal then is transferred and processed to a digital signal in MCA so that a user can access to the signals.

In general, roles of radiation detection system components other than a detector are identical at some extent, so it is crucial to choose an appropriate scintillator for a specific radiation environment. For a high energy neutron detection in high-gamma environments, a fast organic scintillator with a PSD capability would be an effective choice. A stilbene crystal is composed of high concentration of hydrocarbon which allows a neutron to interact with hydrogen even at high energy with (n,p) scattering, by transferring partial energy of neutron to hydrogen. Scattered proton deposits its energy while propagating through the material, resulting a scintillation light pulse shape different from a light pulse different from gamma photon incident [16]. Moreover, small density of the scintillator allows relatively less interaction with gammas and X-rays than inorganic scintillators. Intrinsic properties of stilbene scintillator allow to take advantage in measuring fast neutrons in high noise

environment with gamma and low energy neutrons when an appropriate shielding is applied.

Another scintillator used in this research is a 1" lanthanum bromide crystal doped with cerium (LaBr3:Ce). Different from stilbene, it is utilized to detect gamma rays generated from the target by the same reaction. LaBr3:Ce composes of inorganic materials with higher atomic masses, being less sensitive to neutron incidents. As well as its high sensitivity to gamma ray, risetime of its light pulse is one of the fastest among inorganic scintillators almost comparable to organic scintillators.

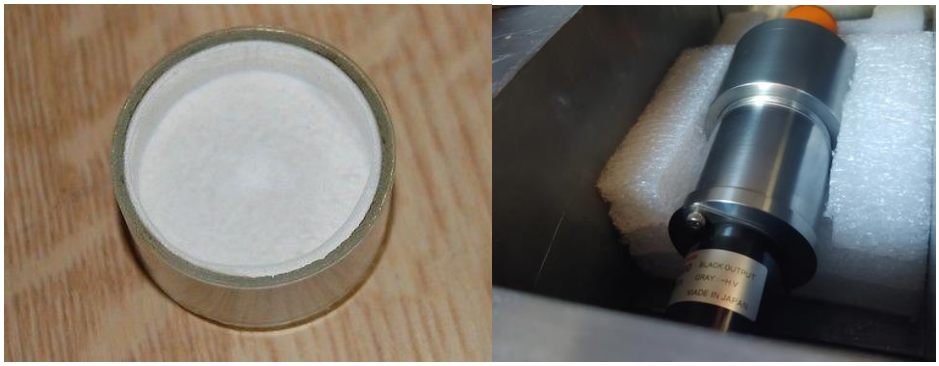

Figure 2.4. (a) 1" LaBr3:Ce scintillator crystal and (b) LaBr3:Ce gamma detector with R1924A Hamamatsu PMT.

Table 2. Properties of scintillators used in the experiment

Scintillators	Materials	Risetime	Detection	Light Yield
Stilbene	Organic	5 ns	Neutron	10,700 p / MeV
LaBr3:Ce	Inorganic	25 ns	Gamma	63,000 p / MeV

A scintillator must be coupled to a photomultiplier module to perform as a radiation detector because scintillation light itself cannot yield sufficient amount of light by single particle incident. A PMT receives light with a photocathode, and converts received light into an electronic signal. A PMT can either output a signal in either current or voltage signal depending on its type, but in this research voltage output type is chosen to process signal as both single pulse counting and spectroscopy

with charge integration method. The 1" stilbene is connected to Hamamatsu H11934-100 PMT and the LaBr3: Ce is coupled to Hamamatsu R1924A PMT with E2924 PM base. Some of their relevant specification is listed in table 3, and Fig 2.5 (a) and (b) is pictures of PMTs before detector assembly [17, 18].

Table 3 Properties of PMTs coupled to the scintillators

PMT	Gain	Rise time	Transit time	Quantum Efficiency
H11934-100	1.2 x 10^6	1.3 ns	5.8 ns	35%
R1924A	2.0 x 10^6	1.5 ns	17 ns	26%

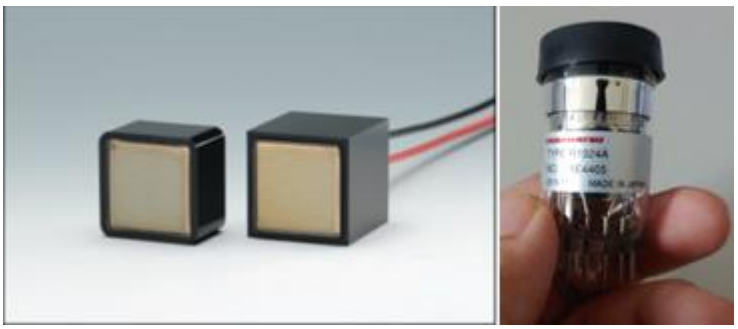

Figure 2.5 (a) H11934-100 PMT module provided by Hamamatsu product page, and (b) R1924A PMT before assembly to PM base.

A choice of MCA can be crucial because it may determine availability and accessibility of data collected by radiation detector. Insufficient sampling rate, lack of RAM memory capacity, and low bandwidth would result limitation of data collection due to loss of signals when fast data processing is required. The experiment is expected to have high emission of gamma, from several hundreds of kilo count per second (KCPS) to few mega count per second (MCPS) at maximum. As substantial amount of signal pileup is expected in this environment, signals must be collected from its raw output from the detector and then processed with a pileup rejection method. Caen DT5751 digitizer is a suitable solution for such acquisition, as it provides sufficient sampling frequency (1 GHz, 2 GHz selectable) for a stilbene

detector with large enough capacity of RAM to record a full waveform up to 1.835 ms when operated at 1 GHz sampling rate. DT5751 is provided and operated from KOMAC with a customized DAQ software made by Pilsoo Lee in KAERI. Fig 2.6 (a) and is a picture of DT5751 and table 4 is its specification provided by Caen [19,34].

Figure 2.6 Picture of DT5751 digitizer, desktop type

Table 4. Specification of DT5751

Instrument	DT5751
Sampling Frequency	1/(GHz/s)
Memory Depth	1.835/Mpts
Dead time	0/μs
Band Width	500/MHz
Sensitivity	1/(mV/div)
Weight	680/gr
Price	50/K

Another substitutional digitizer utilized in this research is a Caen N6725 model. It provides mostly the similar functionality with dt5751, but N6725 provides 250 MS/s sampling rate with 640,000 sampling storage per channel. Both of the digitizer provides sufficiently fast sampling rate and large RAM storage to record full waveform from LaBr3:Ce and stilbene detectors during 500 us of beam pulse width [20]. Digitizers for the full waveform recording is provided by KOMAC facility, and use of each digitizer is determined depending on its availability at that time.

2.2.2. Preliminary Neutron Measurement

Preliminary measurement with single neutron detector is implemented to observe brief detection environment during neutron generation operation. A 1" stilbene detector is utilized. As discussed in the section above, stilbene contains a high concentration of hydrogen atom which provides a n-p scattering cross section to fast neutrons. Fig. 2.7 shows cross sections with different reactions. At range from 1 – 100 MeV, n-p elastic scattering cross section exists continuously. When a neutron interacts with a hydrogen atom inside, they exchange energy depending on their collision angle.

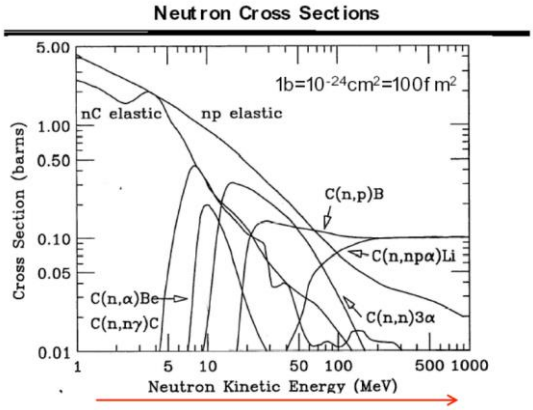

Figure 2.7 Fast neutron cross sections with different reactions

Due to its nature of scattering, the incident energy is not directly reflected by the detector except when a neutron collides with a head-on angle. Lower angle scattering is relatively frequent then a head-on collision, so even when a monoenergetic neutron is detected, a continuous spectrum is expected with such detector. Fig 2.8 is a neutron histogram of 2.4 MeV monoenergetic neutron source measurement with the same stilbene detector at D-D neutron generator in KAERI. X-axis is an arbitrary unit representing energy deposited in the stilbene detector, and y-axis is their counts. Therefore, the measurement is done to verify existence of high energy neutron and to estimate flux of neutron incoming towards detector.

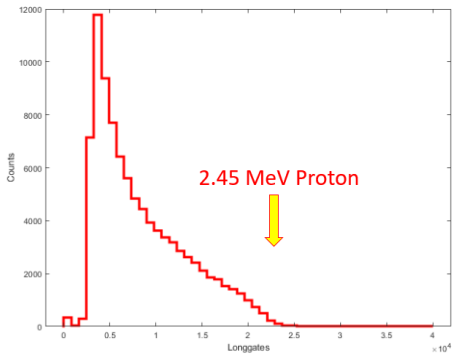

Figure 2.8 Neutron histogram with d-d neutron generator in KAERI

In this measurement, proton accelerator is operated at 0.5 kW with 0.5 uA average current, due to a harsh signal pileup appeared in the detector at 25 m away from the copper beam dump, where the furthest a detector can be placed keeping a countrate of detector be the lowest. The accelerator tunnel length from the beam dump is 31 m, but backscattered gamma rays from its backside wall irradiated by neutrons and gammas also are contributing rise of the detector's noise level. A simplified diagram of the circumstance surrounding beam dump and neutron detector is shown in Fig. 2.9.

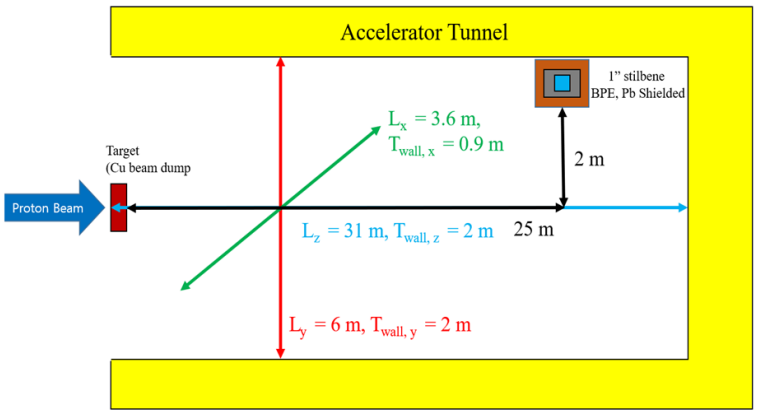

Figure 2.9. Top view of the measurement setup in the accelerator tunnel.

In order to even lower its noise level of the detector from gamma and low energy neutron incident to stilbene detector, stilbene detector is shielded with double layer of 5 x 5 x 10 cm lead blocks inside and 5 % borated polyethylene (PE) blocks

outside to entirely encircle the detector. At the same time, 5 mm slit is left open in the front side of the detector. Pictures of the shielded detector setup is shown in Fig 2.10.

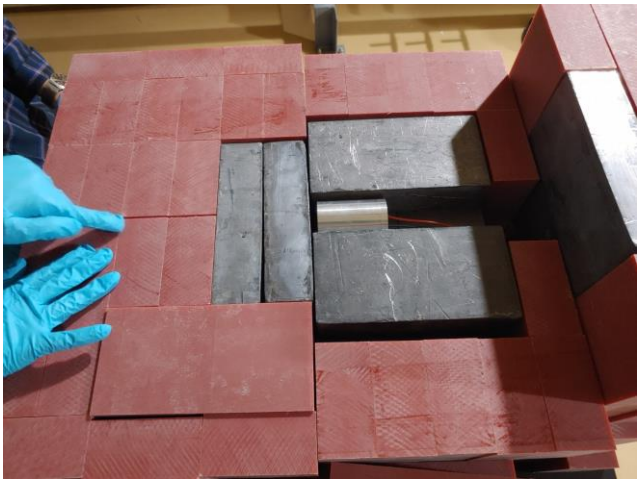

Figure 2.10. Setup of the stilbene detector shielded with borated PE and lead blocks.

Bias voltage is set at 650 V and length of the signal wire is approximately 10 m and connected to a Caen V1751 digitizer, which performs the same feature with dt5751 model discussed above, but is the powered by a VME crate. It is remotely controlled outside of the accelerator tunnel and operated by KOMAC readout software to obtain a full waveform during each entire beam pulse width. Fig 2.11 is a sample acquisition of detector signal during a beam pulse width of 250 us. X axis represents a time sample corresponding to its sampling rate, and y axis represents detector's voltage output in mV. Then the signal is processed with PSD method to separate neutron signal from gamma signal and binned to draw an energy histogram by neutrons only.

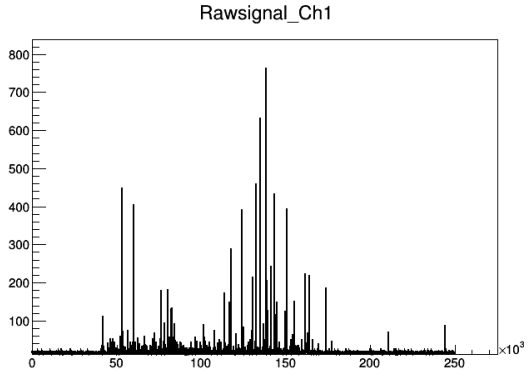

Figure 2.11. A raw waveform signal from the stilbene detector during a beam pulse.

Posterior to the measurement above, another experiment is carried with two scintillation detectors to measure the maximum energy of neutron created by 100 MeV and 69 MeV proton irradiation to beam dump. Energy measurement is conducted by a gamma flash type time-of-flight (TOF) spectroscopy, which measures the time that a neutron generated from its source and reaches a neutron detector located at a certain position. A gamma flash detector is located near to the neutron target to indicate the time when a proton pulse is irradiated to the detector. The neutron generated time is estimated with following:

$$t_{ngen} = t_{\gamma flash} - t_{\gamma tof} \quad (2.1)$$

t_{ngen} represents a time when the pulse is irradiated and a neutron is generated, and $t_{\gamma flash}$ is the start of a scintillation pulse started in a gamma flash detector. By subtracting $t_{\gamma tof}$ which is obtained by dividing a distance between the target and detector with the speed of light. Then, neutron signals detected by a second scintillation detector is collected with a synchronized time. Neutron time of flight is obtained by tracking each pulse's incident time subtracted by t_{ngen}. Finally, neutron kinetic energy can be obtained with t_{ntof} and relativistic kinetic energy equation described in equation (2.2) and (2.3).

$$v_n = \frac{L_{source-detector}}{(t_{ngen} - t_{npulse})} \quad (2.2)$$

$$KE_n = m_0 c^2 \left[\frac{1}{\sqrt{1-\frac{{v_n}^2}{c^2}}} - 1 \right] \qquad (2.3)$$

2.2.3. Time-of-Flight Neutron Measurement.

Neutron time-of-flight method is widely utilized in various facilities providing fast neutron sources for its direct measurability of neutron energy without assumption [21,22]. However, it requires a proton pulse width considerably shorter than its time-of-flight at its maximum energy as the gamma flash time only indicates only the start of a neutron generation. At 100 MeV neutron measurement condition with 25 m time-of-flight path, it takes 197 ns to reach the detector from its place of generation. Consequently, the system requires 20 ns of proton beam pulse width to acquire energy resolution of 10 % at 100 MeV, while the proton beam accelerator in KOMAC can only provide beam pulse longer than 20 us at this moment. A total spectrum cannot be obtained with the long pulse, so as the system is composed to measure only the maximum energy of neutron by detecting the first incoming neutron signal at the neutron detector. Fig. 2.12 is a picture which shows a gamma flash detector located near to the beam dump.

Figure 2.12 Gamma flash detector placed near to the beam dump.

As a gamma flash detector, LaBr3:Ce scintillator is used because of its excellent gamma sensitivity, fast signal rise time, and high light yield to make a very sensitive time indicator. To discriminate a single gamma incident by a random radiation from the environment, the detector is placed as closest as possible to generate a large bulky

signal when proton beam is irradiated. A 1” stilbene neutron detector is placed at the same position with the previous measurement setup so that a neutron can travel 25 m flight path across the tunnel, while being able to process scintillation light pulse signals pulse-by-pulse. Fig 2.13 is a conceptual diagram of neutron TOF setup in this measurement.

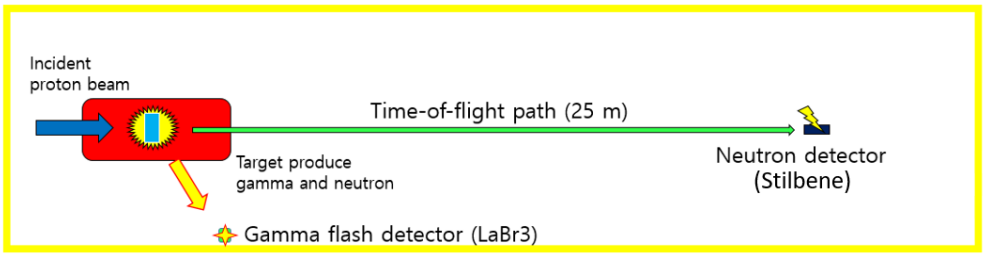

Figure 2.13. A conceptual diagram of the neutron TOF setup

Time synchronization between the two detector is crucial factor in measuring nanosecond-scale TOF. The gamma flash and stilbene detector is connected to a single digitizer so that they share the same clock for time indication, and signal cable lengths and electron transit time between two different PMT is considered in correction of time synchronization. Then, pulse start time at gamma flash signal and neutron detector pulse signal is compared to obtain a generated neutron’s flight time, as demonstrated in Fig. 2.14.

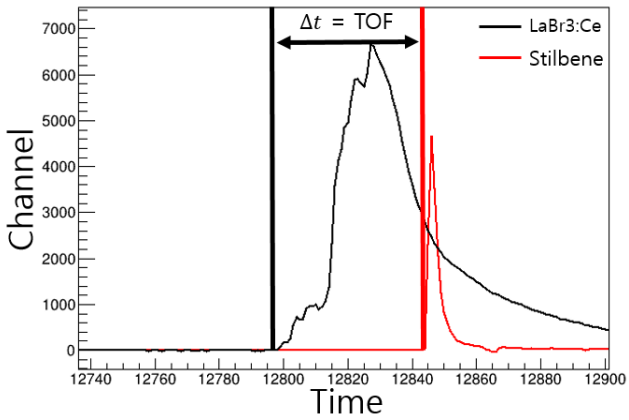

Figure 2.14. Two-channel time of flight measurement example for this experiment

As shown in Fig 2.14. time difference between pulse start point of each signals is obtained and collected for each proton beam pulse. Time axis represents each time sample with the digitizer's sampling rate, and channel axis represents a voltage strength in arbitrary unit.

2.2.4. Data Analysis.

Throughout the analysis, whole process is calculated in ROOT software freely distributed by CERN [23], an object-oriented data analysis framework operated with C++, alongside with MATLAB software [24]. While ROOT provides accessibility to a structured dataset so-called a tree and allows a faster data processing and efficient memory management compared to other data frameworks operated with higher language, MATLAB provides a simplicity and highly sophisticated library specialized for numerical analysis. KOMAC readout software utilizes root file formed as a tree structure so that a smaller sizes of data can be provided than csv file, one of the most commonly used data format.

Some special organic scintillators designed for neutron detection, such as a stilbene detector, is able to distinguish scintillation light pulse generated by neutron and gamma incident. As they produce different secondary particles when colliding with materials inside the stilbene detector, light pulse shapes produced by them are different as well. Especially a pulse from neutron tends to have longer tail than one generated from gamma due to the mass difference and consequent stopping power difference inside of the medium. Different stopping power causes difference in density of excitation of electron level, which leads to have different electron density in excitation states that the scintillator contains. Electron density difference in excitation states difference also signifies different electron decay time to lower level, generating different pulse tail in the end. Fig 2.15 illustrates tail differences by each incident particles [16].

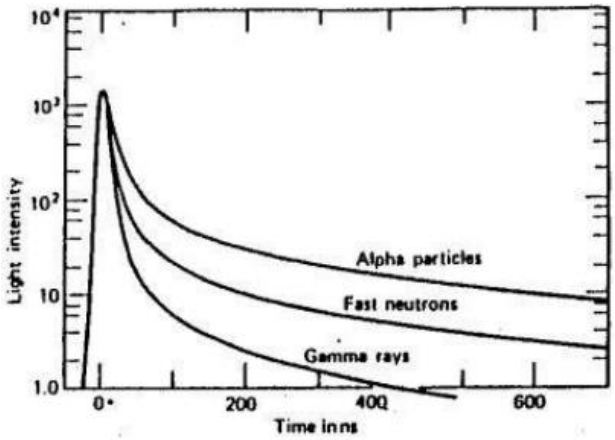

Figure 2.15. Tail differences generated by an organic scintillator between alpha, neutron, and gamma rays.

Particle discrimination with tail difference is commonly called pulse shape discrimination (PSD), and it can be parametrized as following equation:

$$\text{PSD Value} = \frac{\int_{pulsestart}^{longgate} Vdt - \int_{pulsestart}^{shortgate} Vdt}{\int_{pulsestart}^{longgate} Vdt} \qquad (2.4)$$

Long gate and short gate is defined as the time of where a pulse is integrated from start of a pulse. Integration of voltage signal over a long gate is a total energy deposited by a secondary proton and integration over a short gate is a partial energy of its signal. Subtraction of these two signifies the difference of tail surface area, and by dividing the tail surface area into the total energy, tail difference ratio by each incident particle is obtained.

To conduct such operation, integrity of pulse signals from the measurement setup must be provided in advance. KOMAC readout software provides an entire waveform recorded during the beam irradiation by each beam pulse, so data processing from raw data signal is carried out by following procedure. From a raw signal exemplified in Fig. 2.11, scintillation light pulses over a threshold of 22 ch. is sliced out of the waveform and aligned, as shown in Fig. 2.16.

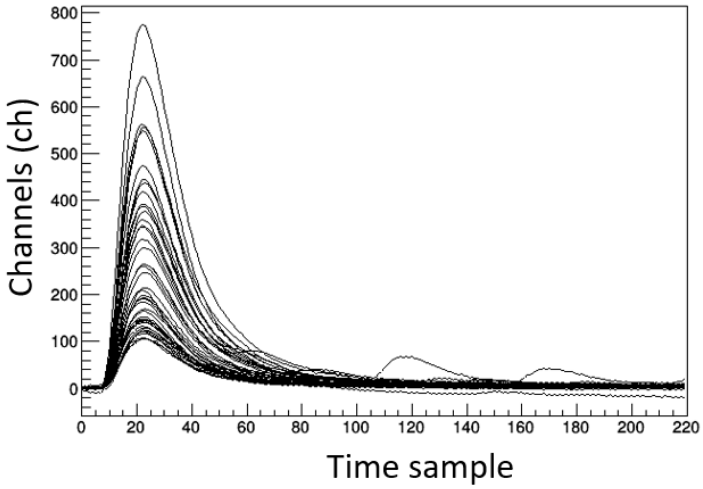

Figure 2.16. Detector signals collected from a raw signal over 10 proton beam pulses.

As it can be observed in Fig. 2.16, some of pulses' tail signals is contaminated due to a pulse pileup. When another particle randomly incidents within a time period shorter than a scintillator pulse width, tail signal can be contaminated, which causes an error in PSD processing. Therefore, elimination of piled-up pulses is implemented in the pulse collecting algorithm so that only a pure signal is collected. Signals aligned with pileup rejection is shown in Fig 2.17. It is clearly shown that a pileup signal is eliminated with the algorithm. In total, 8.5 % of total signal is eliminated due to pileup in the tail at average countrate of 153 KCPS.

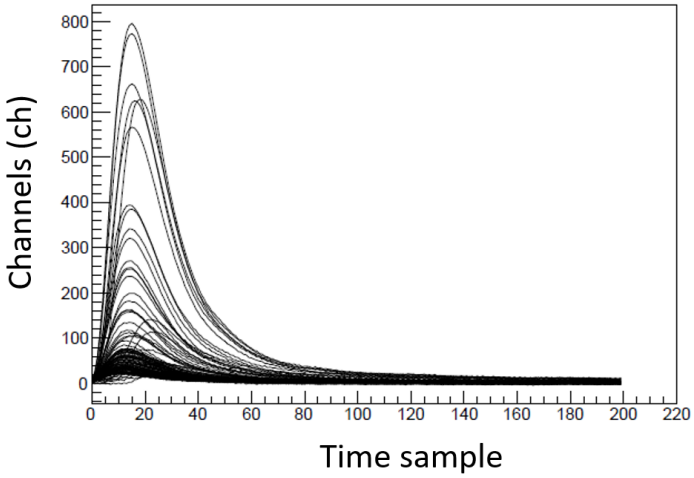

Figure 2.17. Pulses collected over the same 10 proton beam pulses with pileup rejection.

After the elimination of signals, PSD method is processed for all collected signals. Long gate and short gate is set at 60 ns and 30 ns respectively, and the signal is plotted into a conventional 2-d histogram. In fig 2.18, y axis and x axis represents PSD value and pulse height of the signal respectively, and its color represents the intensity.

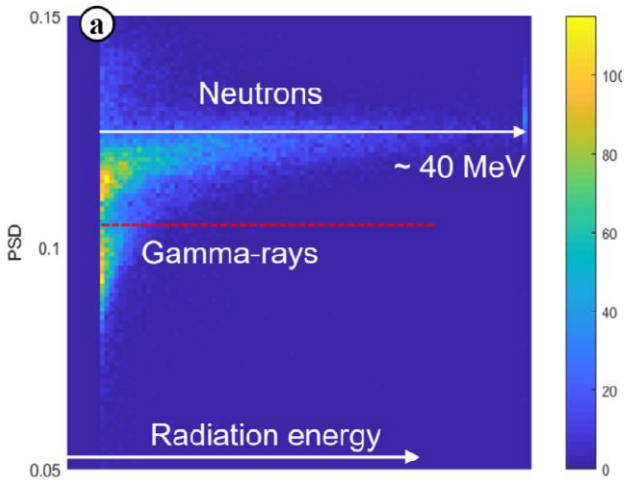

Figure 2.18. 2-D PSD histogram plot from signals detected through 1000 shots of 100 MeV proton beam.

As it can be seen in the figure above, gamma ray and neutron signals are visibly separated with a PSD value at 0.11. A pulse height values roughly are considered as the deposited energy on scintillator, as the scintillation light output is assumed to be proportional in this research. Under the assumption energy calibration is conducted with a monoenergetic neutron discussed above, by selecting an edge of neutron spectrum to be 2.45 MeV neutron energy deposition. Collecting its neutron signals is conducted with the same PSD method with above. Fig 2.19 is a 2-d PSD histogram of neutrons from the energy calibration measurement.

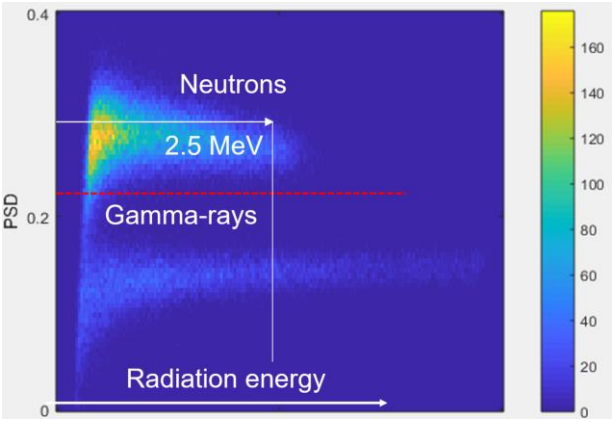

Figure 2.19. 2-d PSD histogram plot drawn with signals collected from d-d neutron source.

The bias voltage in this measurement is set at 800 V. It is configured 150 V higher than that of measurement setup with 100 MeV neutrons, and therefore the gain difference is adjusted in calibration with typical gain data provided by Hamamatsu [18].

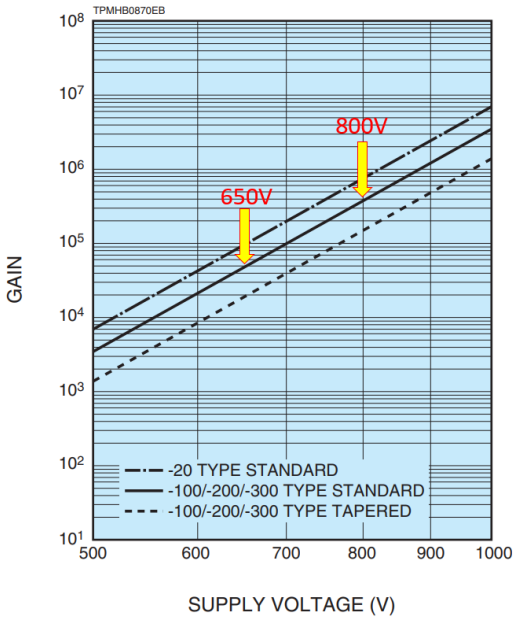

Figure 2.20 Typical gain of Hamamatsu H11934 series PMT.

Neutron TOF measurement data contains two different signal output from LaBr3:Ce gamma flash and stilbene neutron detector. Two time-synchronized signal is aligned in a same time axis with internal clock of a digitizer. Indication of gamma flash time is selected with a pulse signal distinguishably high and bulky. A raw waveform is presented in Fig 2.21. The waveform described by black and red lines represents signal output from LaBr3:Ce and stilbene respectively.

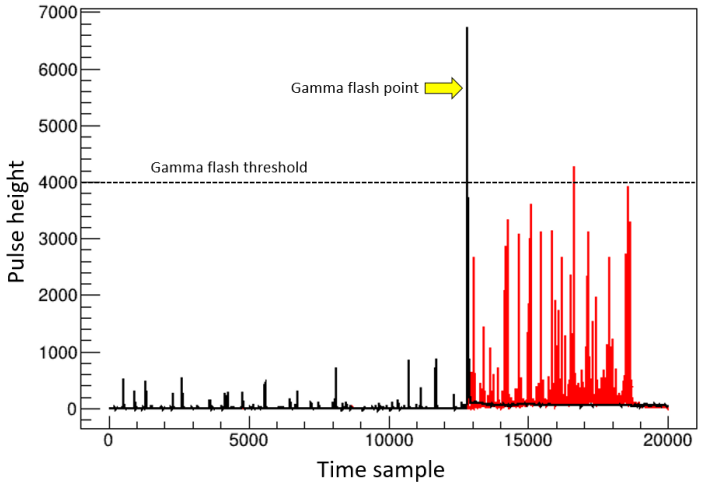

Figure 2.21. Raw waveform with two detectors in synchronized time axis.

As it is recorded by a R6725 digitizer with 250 MS/s sampling rate, a time sample signifies 4 ns in this waveform. It can be seen in the figure that multiple gamma incident is present even before beam irradiation due to gamma radiation by activation of the beam dump. Therefore, gamma flash point is determined a signal exceeds pulse height threshold higher than 4000. Due to saturation of PMT by gamma flash radiation, PMT signals after gamma flash point is immediately faded. Consistency of gamma flash time is verified with an external trigger from the proton accelerator. The x-axis value 0 is when the proton accelerator trigger is activated in Figure 2.22.

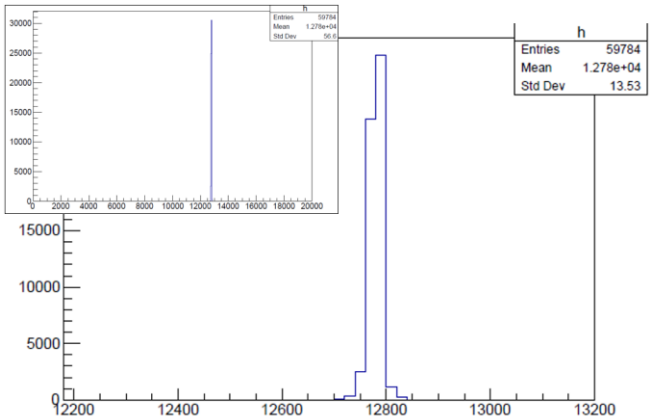

Figure 2.22. Triggered activated time indicated by gamma flash by each beam pulse.

Trigger time is collected by each beam pulse and binned in a histogram in Fig 2.22. it is evident in the figure that all trigger time is located within a range of 50 ns. Considering a fluctuation of external trigger generated by the accelerator, gamma flash trigger time would be assessed as a consistent source for time tagging.

PSD is again performed for the first incoming signal detected by stilbene scintillator, since it is necessary to identify whether it is generated from a gamma or a neutron incident. Any signal over a threshold of 300 is considered as a valid signal and processed with PSD and plotted on 2-d histogram to observe a distribution of gamma and neutron signals under the TOF experiment condition. Fig 2.23 is the PSD plot of the first incoming signal from stilbene detector after gamma flash trigger time. The PSD plot is collected over 120000 proton pulses with 69 MeV Energy.

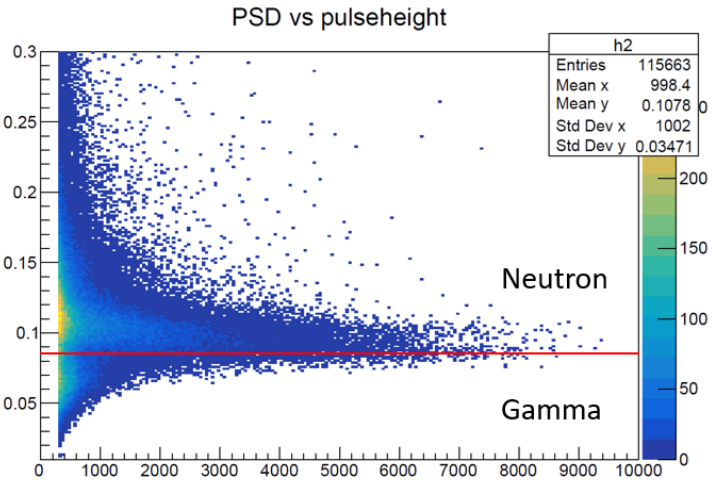

Figure 2.23 PSD plot drawn with 69 MeV proton beam pulses.

It can be observed in the figure that the neutrons are separated from gamma signals from PSD values surpassing 0.085. The first incoming signal is then drawn on a histogram for its time difference from gamma flash trigger Fig. 2.24. The adjustment of PMT electron transit time is included in the figure. Gamma flash distance is set at 1 m and detector location is calculated as 25 m from the dump. X-axis indicates time-of-flight of first incident particle, calculated by equations below. PMT transit time is set at 17 ns for PMT1 and 5.8 ns for PMT2.

$$t_{protonincident} = t_{\gamma flash} - \frac{\Delta x_{dump-\gamma flash}}{c} - t_{PMT1transit} \quad (2.5)$$

$$t_{tof} = \left(t_{firstsignal} - t_{PMT2transit}\right) - t_{protonincident} \quad (2.6)$$

Without PSD process, t_{tof} will include gamma signals directly or indirectly transported to the neutron detector. By observing an innermost edge of the TOF histogram, a gamma ray generated from the proton incident directly delivered to the neutron detector will be observed, and the time of flight from the signal must be 25 m divided by the speed of light.

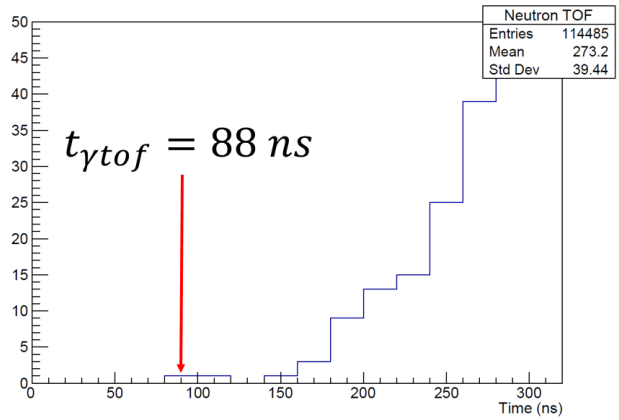

Figure 2.24. TOF histogram of first incoming signal without PSD at 69 MeV proton energy.

The displayed TOF histogram clearly shows the time of flight is distributed shorter than a that of a 69 MeV neutron traveling 25 m flight path. Gamma time-of-flight of 25 m path is approximately 83.3 ns in calculation, and therefore the time edge of gamma rays for this TOF system is formed ~ 5 ns difference from the ideal condition. Measurement data from 60000 proton beam pulses with energy of 100 MeV is drawn in a histogram altogether. Fig. 2.25 is a TOF histogram for 180000 proton beam shots of first-incoming pulse without particle type discrimination for a better statistic. The figure clearly draws a line which drops to zero at 80 ~ 100 ns time range.

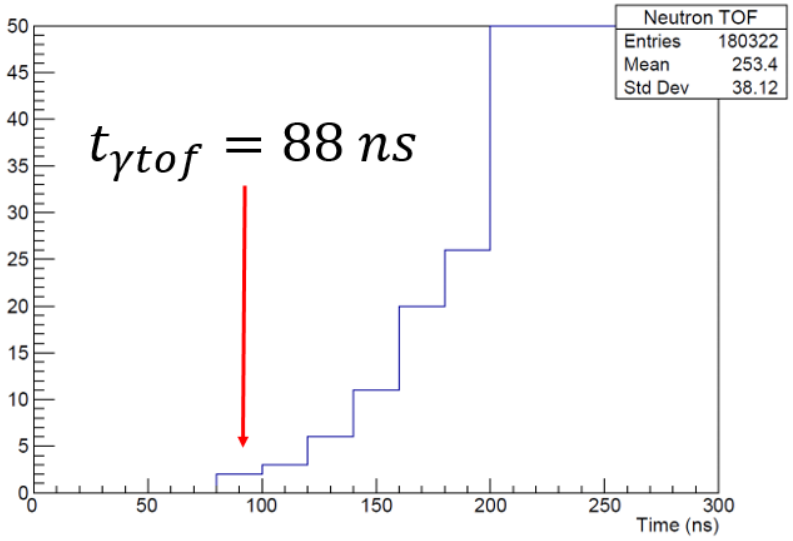

Figure 2.25. TOF histogram for all 100 MeV and 69 MeV proton beam pulses put together.

It is essential to identify an appropriate range for gamma-neutron discrimination. As seen in the PSD plot above, a border between neutron and gamma is not clearly shown due to harsh signal pileup by presence of dominant gamma and thermal neutron incidents. As a result of several trials, PSD value between 0.085 and 0.15 with a pulse height threshold of 250 is selected to be parameters for the neutron selection. At the same time, any signals with pulse height of 2000 is considered to be caused by a fast neutron incident. Fig. 2.26 is TOF histogram with neutrons only at 69 MeV and 100 MeV.

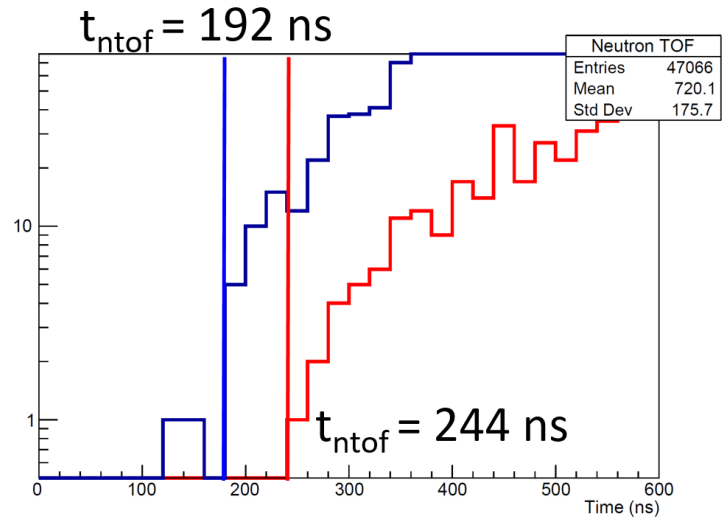

Figure 2.26. Time of Flight comparison between signals from 69 MeV and 100 MeV proton pulse.

It can be recognized that errors are present in the histogram. Some of TOF signals are above their flight time threshold for their energy. It is assumed to be that the gamma flash time is irrelevantly evaluated so that TOF of the signal is underestimated. Some of the trigger did not have enough amount of gamma incident in the beginning, so that the pulse did not built up at a proton incident time.

With these parameters, the signals time of flight is converted with neutron energy with relativistic kinetic equation discussed in section above. Neutrons only in Fig. 2.27 for 100 MeV and 69 MeV proton energies in respective order. It can be seen in the histogram that the neutron signal vanishes at 90 MeV and 60 MeV for each type of beam pulses. It is an expected result from the TOF spectrum because the neutrons at their energy close to proton energy before p-n conversion is highly unlikely to be detected. Spectrum shape for 69 MeV and 100 MeV is obtained with a Geant4 simulation to verify. A rapid decrease of neutron yield at the corresponding energy can be seen in Fig 2.28. In conclusion, TOF measurement evidently discern neutron energy generated from 69 MeV and 100 MeV proton pulses, observing the neutron energies at 60 MeV and 90 MeV respectively.

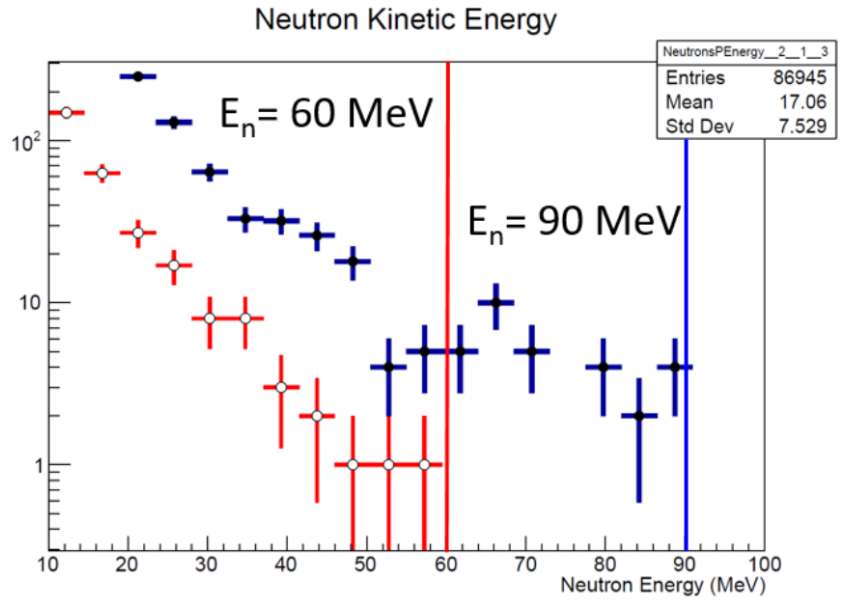

Figure 2.27. Neutron energy calculated by time of flight acquired from Fig. 2.26.

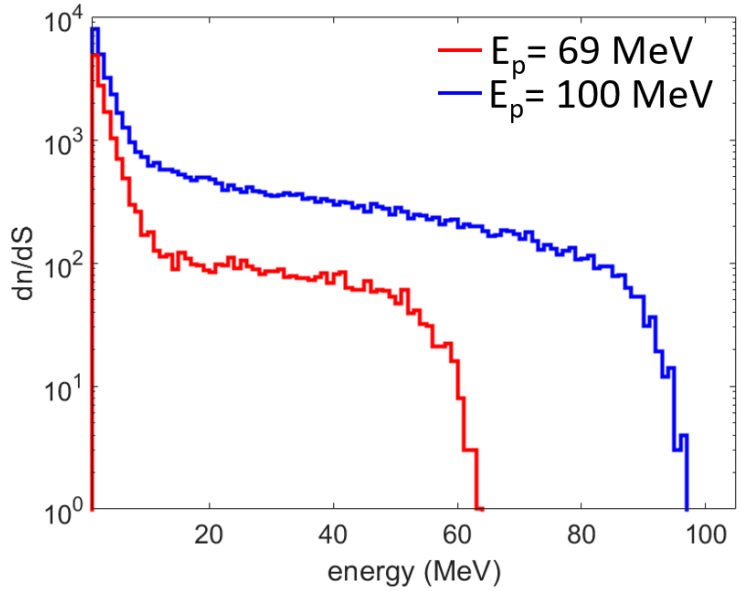

Figure 2.28. Spectrum of neutron yield at zero degree simulated by Geant4.

Chapter 3. Monte-Carlo Simulation

3.1. Geant4 Monte-Carlo Toolkit

In this thesis, all simulations are conducted with Geant4.10.3. Geant4 Monte-Carlo toolkit is one of the most widely used Monte-Carlo code for radiation assessment of various situations. The name Geant4 signifies particle Geometry and Tracking of particles by Monte-Carlo method [25]. Geant4 in default provides wide range of physics models and cross sections for particles from its energy of fractions of eV to TeV. Moreover, it is a freeware with a license statement with minimal restrictions of use. The code is operated in C++ language and provided as a source code. To construct a simulation, a user is required to build a program from its source code with vast amount of libraries which Geant4 provide, so one is asked to have a certain level of proficiency in C++ and programming. On the other hand, a user is accessible to almost all processes of a simulation and collect any type of data desired. Due to its versatility, the code encompasses almost all of processes that is expected to occur in any kind of experiment.

Main purpose of simulations conducted in this research is to verify its flux and energy histogram shape that would appear on the detector signal by 100 MeV proton irradiation. It can be accomplished by arranging a simulation set with a minimal simplification and assumption on its processes for the situation that is desired to replicate. While replication of environmental circumstances and structures being extremely complex and painstaking, minimizing assumption of processes on simulation can be achieved by simulating all major processes in single simulation. Geant4 provides all major physics libraries concerned in this simulation [26], and therefore it is possible to imitate processes of neutron generation by proton irradiation, neutron transport, and detector response with scintillation processes, so that the result of the simulation can be directly compared with result from the experiment.

3.2. Neutron Generation Simulation

Neutron generation simulation is a priori conducted to observe neutron generation behavior when 100 MeV protons are irradiated to a target. For the physics models chosen for neutron generation at 100 MeV energy range is QGSP_BIC model, which utilizes a binary cascade model at intermediate energy range for hadronic nuclear reactions [27]. Proton-neutron conversion ratio for Cu with full stopping thickness for 100 MeV proton is approximately 0.162, and fraction of fast neutron over 10 MeV energy from generated neutrons is 3.5 %. In case of 0.5 kW average power of proton irradiation, there will be 3.125E13 protons incoming to the beam dump, which corresponds to production of 5.03E12 neutron in total and 1.76E11 neutrons above 10 MeV energy. A 2-d histogram map is drawn for neutron energy spectrum with polar angle in Fig. 3.1, indicating that high energy neutron is highly angle dependent with respect to polar angle theta. Polar angle of 0 lies on an axis along with direction of the proton propagation. Color bar indicates neutron intensity at corresponding parameter.

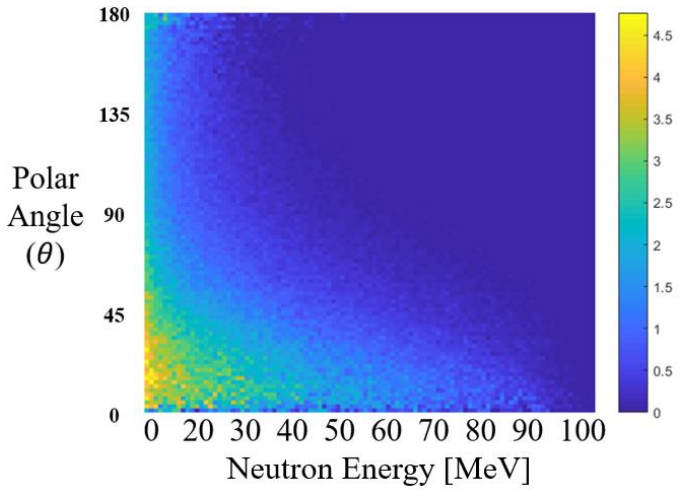

Figure 3.1. Neutron energy and polar angle histogram at a thick Cu target.

3.3. Neutron Transport Simulation

The beam dump and circumstances surrounding the neutron detector is implemented with simplified geometry. Their positions and sizes are measured from the experimental environment same as the first neutron measurement with a stilbene detector discussed in section 2.2.1. Diagram of the configurations is illustrated in Fig. 2.9. The beam dump internal structure, concrete wall thickness and accelerator tunnel dimensions are obtained from CAD drawings provided by KOMAC facility. There were quadruple magnets located in a path between the beam dump and detector and they are also modeled and located in equivalent position. Stilbene detector is located at 25 meter away vertically and 2 meter horizontally. The detector is covered with gamma and thermal neutron shielding blocks. Thickness of each shielding is 5 cm and 10 cm respectively. The beam dump is set at origin, and tunnel geometries only from the dump to detector are brought into the simulation. The 100 MeV proton beam with beam radius of 30 mm is irradiated to the center of beam dump and all other processes associated with neutron generation and transport to the detector is executed. Fig 3.2 is a visualized geometry of the simulation.

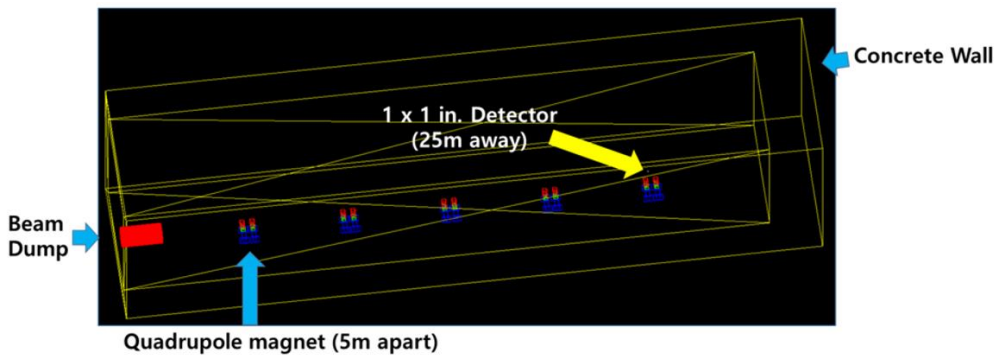

Figure 3.2. Visualized simulation setup of neutron detection environment.

3.4. Detection Simulation.

A special feature that Geant4 provides is that it presents an optical physics model in default. This feature enables a user to simulate detector light output expected from a particle incident, which gives advantage on estimating errors and energy spectrum discrepancy caused by a scintillator's energy resolution by fluctuation and nonlinearity of detector's light output respect to a deposited energy on a scintillator. Physics models implemented for the detector simulation is hadron elastic models for n-p conversion from neutron colliding hydrogen atom, and optical physics model for scintillation and photon transport in the scintillator medium.

In G4Scintillation class in the code, energy deposition on scintillator material is converted with a light yield factor commonly expressed in photons / MeVee. For a stilbene detector, light yield is commonly known to be approximately ~ 10,700 photons / MeVee. A user is also required to arrange decay time components and risetime of a scintillator in order to reproduce a scintillation light pulse similar with an actual output signal from a measurement. Fast, slow decay components, and risetime are set at 4 ns, 22 ns and 5 ns respectively. The light pulse is constructed by binning a scintillation photon transferred out of a scintillation crystal window. Other side of the scintillator is covered with 0.5 mm thick Teflon tape so that scintillation lights are either reflected or excluded from the simulation. Fig. 3.3 is a visualization of Geant4 simulation during a particle incident. Green lines signify trajectories of neutral particles. Any photons coming out of blue surface in the figure is recorded with its time.

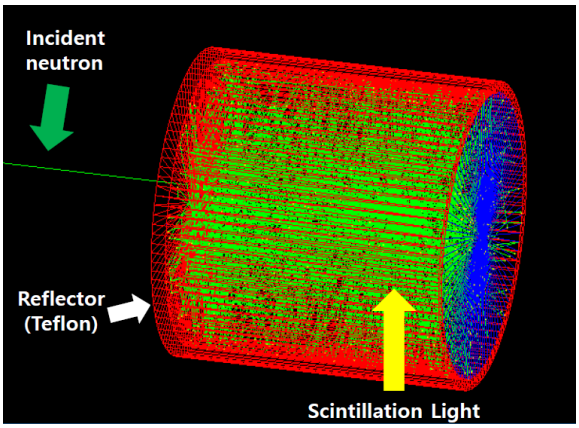

Figure 3.3. A simulation of stilbene scintillation with a neutron incident.

The photons coming out from scintillator medium is binned with 1 ns bin width. Fig. 3.4 is a histogram drawn with a collection of scintillation photons by incidents of neutrons delivered to stilbene detector from beam dump. Time zero is set at when a particle interacts with materials inside the detector. It can be observed that most of the lights are diminished 40 ns after its generation. However, stilbene signal from experiment is expected to be longer than those from simulation, due to absence of third decay time component. In Geant4.10.3, it is unable to put the third time decay constant, but this feature will soon be updated with next release for Geant4.10.7.

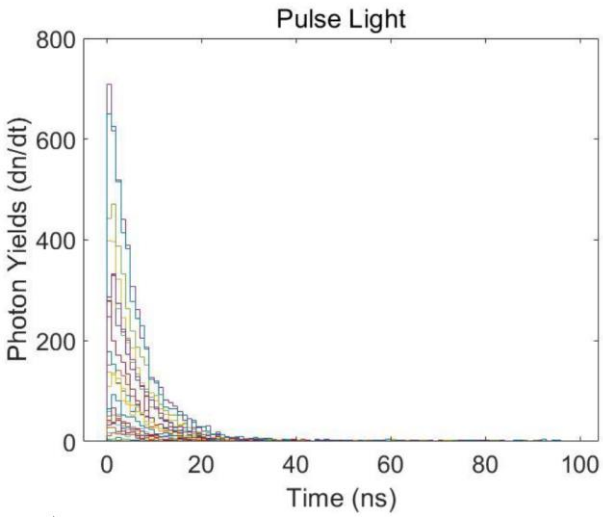

Figure 3.4. Stilbene detector light pulse output simulated by Geant4.

The simulated light pulse is converted into energy value using charge integration method, assuming that light output would be equal to be voltage output from a scintillation detector. The simulation output data also contains incident neutron energy so that amount of scintillation photons can directly be converted to be its energy. The energies from incident neutrons is drawn in a histogram in Fig. 3.5.

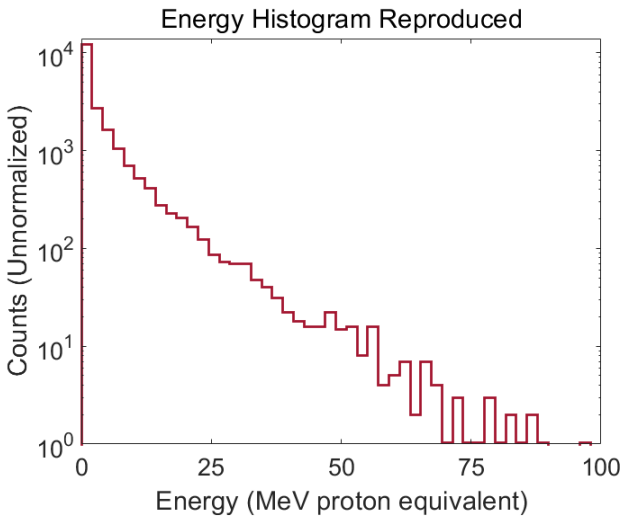

Figure 3.5. Energy histogram of a stilbene detector by neutrons delivered from beam dump in Geant4.

It is observed in the simulation that incident neutron energy above 50 MeV is not correctly reflected to scintillation light output because the propagation length of proton above the energy inside stilbene material surpasses 1 inch. Protons converted from neutrons above 50 MeV escapes from the scintillator and leads to errors in estimation of energy histogram. Therefore, a direct comparison between signals from experiment and simulation is conducted within the range from 10 MeV to 40 MeV.

3.5. Simulation Compared with Experiment.

Reproduced data from the simulation is compared with an experimental data acquired from the same configuration. From a measured PSD plot data same as one discussed in Fig. 2.19, pulses with more than 0.11 PSD value is considered as a neutron signal and redrawn as a neutron energy. Due to dynamic range of detection system, energies below 10 MeV is not included in the evaluation.

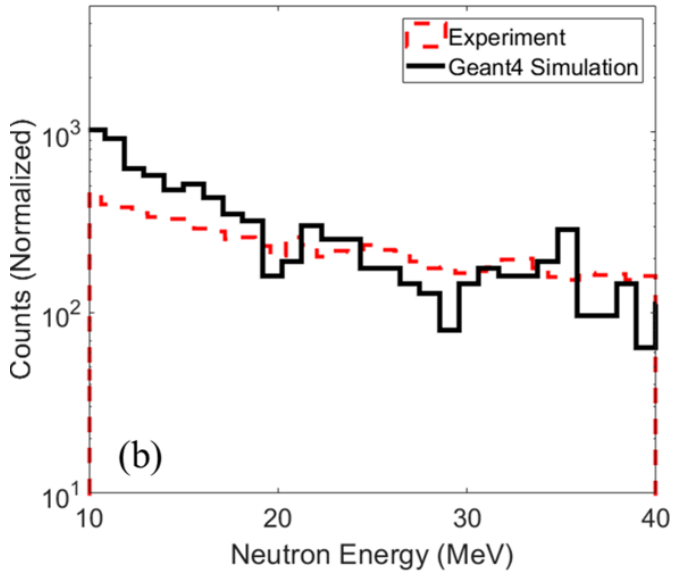

Figure 3.6 Energy spectrum comparison between Geant4 simulation and measurement with the same condition.

Fig. 3. 6 illustrates the comparison between simulation and experimental data. the energy histograms are only compared from 10 to 40 MeV of neutrons. The result shows rough agreement on the differential histogram shape within the detection range under a factor of 2. Measured countrate from the scintillation detector is 300 neutron/s at 0.5 kW operation, where the simulated count rate is approximately 366 neutron/s, which is 22% difference between the two.

Chapter 4. Neutron Target Design

4.1. Neutron Target Material

As discussed in Chapter 1.2, purpose of this study includes building a neutron target to produce atmospheric neutron-like spectrum with a sufficient flux at the irradiation station. It is to be utilized for soft error assessment on various semiconductor devices by neutron irradiation from cosmic ray-induced neutrons, so that it is required to generate a continuous distribution of energy from 1 MeV to 100 MeV with an acceleration factor above 10^8, as suggested by other soft error testing facilities [12]. In addition to such acceleration factor, or equivalently the neutron yield, the energy spectrum of the target-generated neutrons should be considered to be similar to the atmospheric neutrons. Setup for target material is visualized as Fig. 4.1.

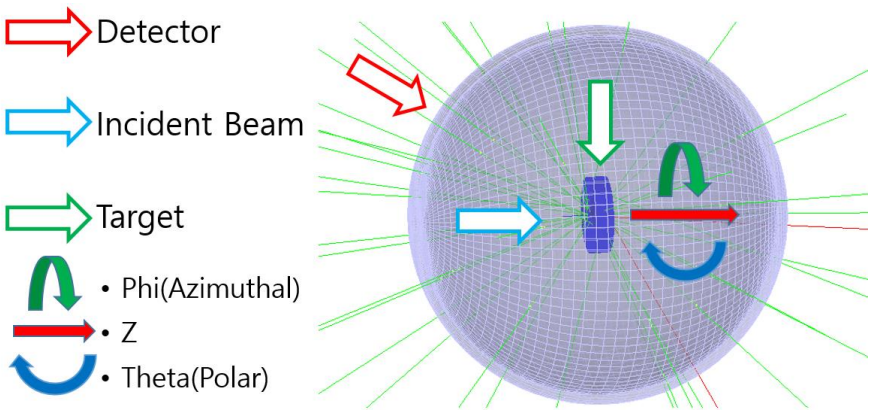

Figure 4.1. Geometry visualization of the simulation arrangement.

Simulation is arranged as the diagram above; Blue disk represents a testing target, and 100 MeV proton beam is irradiated 10mm away from the disk along z-axis (horizontal). Outer sphere illustrates a detective area which collects angular and

energy data from particles passing through the surface. Neutron energy calculation is conducted using the same physics model as in Chapter 3.

Candidate materials are selected among pure metals like Al, Ti, Cu, W, Hg, and Pb which are widely used in accelerator-based neutron facilities for similar purposes [28- 30]. Each material is evaluated two different energy range from 1 to 10 MeV (low energy) and 10 to 100 MeV (high energy) in terms of similarity with the atmospheric neutron spectrum. It is suggested by Baggio et al. that neutrons with energies of 1-10 MeV range contributes approximately 10 % of total SEU, and consequently the materials are assessed with two different energy range with a weight factor of 0.1 for 1-10 MeV and 0.9 for 10-100 MeV.

Irradiation station that will be installed in KOMAC facility is expected to be positioned at 5 m away from the target with polar angle of 7° respect to its z-axis. It is studied in the previous chapter that high energy neutrons are highly dependent on its flight angle, and therefore all materials are assessed with neutron generation at theta = 7°. Fig 4.2 (a) is a scatter plot of neutron yield at 1-10 MeV and 10-100 MeV respectively, and (b) is a normalized neutron spectrum at 10 MeV observed at 7° polar angle from each material.

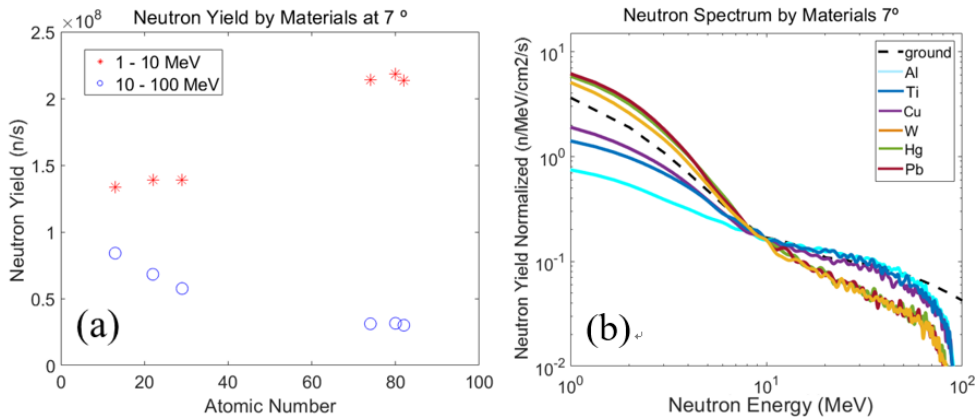

Figure 4.2. (a) Neutron yields at 1 – 10 MeV and 10 – 100 MeV by atomic number, and (b) spectrum differences among target materials.

Fig. 4.2 (a) shows the neutron yield of each energy group depending on the atomic number of target materials calculated at 7° away from the target. It is clearly observed that the neutron energy generated by the impact of 100 MeV proton beam depends strongly on the atomic number (Z) of target material. It is obvious that high-energy neutrons are more preferably produced for targets made of low-Z material because the protons impinging on the target lose their energy mostly by the interaction with atomic electrons whose number is proportional to Z number. For the same reason, the targets made of high-Z material are suitable to produce low-energy neutrons. Fig. 4.2 (b) illustrates the comparison between the neutron energy spectra calculated for various target materials irradiated by 100 MeV proton beam and the reference spectrum. All neutron spectra are normalized to the neutron yields at 10 MeV neutron energy. The change in the shape of neutron spectrum is clearly seen for different target materials.

In order to evaluate the spectrum shape in comparison with the atmospheric neutron spectrum, we introduce a new parameter called the effective overall deviation, defined by

$$\sigma = \sqrt{a\sum_{i=1}^{10}(x_i - \bar{x}_i)^2 + \; b\sum_{i=10}^{100}(x_i - \bar{x}_i)^2} \quad (4.1)$$

where x_i and $\bar{x}_i$ are the differential neutron yield of *i*th energy bin for each target material and the atmospheric neutron flux at *i*th energy bin, respectively. The weighting factors a and b are determined to be 0.1 and 0.9 according to the energy-dependent contribution to the occurrence of soft errors [6]. Table 1 summarizes the effective overall deviation for the candidate target materials. From this result, Cu is chosen to be the most proper material as a target for 100-MeV proton accelerator for producing neutron energy spectrum similar to the atmospheric neutrons.

Table 5. Calculated average deviation from atmospheric spectrum by materials.

Materials	Deviation 1 – 10 MeV	Deviation 10 – 100 MeV	Unweighted overall deviation	Effective Overall deviation
Al(Z=13)	3.31	0.191	3.31	1.061
Ti (Z=22)	2.46	0.204	2.47	0.801
Cu(Z=29)	1.91	0.221	1.92	0.638
W(Z =76)	1.65	0.405	1.70	0.649
Hg(Z=80)	2.64	0.386	2.67	0.911
Pb(Z=82)	3.05	0.395	3.08	1.035

4.2. Neutron Target Design.

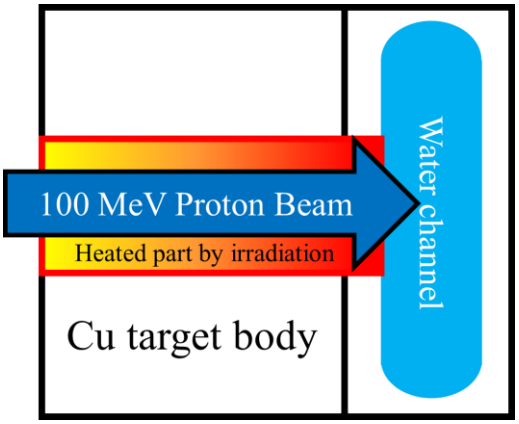

Figure 4.3. Conceptual model of the target with cooling water channel

Fig. 4.3 represents a simplified model of the target assembly consisting of the Cu target body and the cooling water channel attached to the backside of the target. Main idea of the design involves that the 100 MeV proton beam fully penetrates through the Cu target medium so that it stops in the middle of the cooling water. This concept allows an effective heat removal of 2-kW power of proton beam irradiation to the Cu target as well as a longer target life expectancy due to prevention of possible blistering when the proton beam is fully stopped and remains inside the Cu target. However, the change in thickness of Cu target body and the presence of water channel on the beam path might affect the neutron yield and energy spectrum at the irradiation station. To minimize this effect, it is desired for the proton beam to attenuate most of its energy inside the Cu target body, so that the required thickness of water channel for the proton beam to entirely stop must be as short as possible.

In order to find the optimum thicknesses of the Cu target body and water channel, the stopping position of the 100-MeV proton beam and its straggling distance are calculated for various thicknesses of Cu target body, as summarized in Table 2. The thickness of the water channel is determined by adding the straggling distance to the stopping position of the proton beam in water. The calculation result reveals that the

optimum thicknesses of the Cu target body and the water channel are 13 mm and 9.1 mm, respectively. With the consideration of engineering margin, we finally determine the thicknesses of water channel to be 10 mm. Based on this simple geometrical consideration, the engineering design has been carried out for the target assembly to be accommodated at the end of proton beam line, as represented in Figs. 4.4(a) and 4.4(b).

The overall stopping characteristics of the 100-MeV proton beam impinging on the target assembly is depicted in Fig. 4.5. It is clearly shown that the stopping power is rapidly decreased at 13 mm where the proton beam fully penetrates Cu medium and enters the water channel. The proton stopping position indicated as a dashed line in Fig. 4.5 signifies that 100 MeV protons irradiated to the target are safely stopped in the middle of the water channel.

Table 6. Proton stopping position with different Cu body thickness

Cu Body Thickness (mm)	Proton Stopping Position in Water (mm)	Straggling Distance (mm)	Water Channel Thickness (mm)
10	22.3	4.1	26.4
11	16.6		20.7
12	10.8		14.9
13	5.0		9.1
14	Not penetrated		

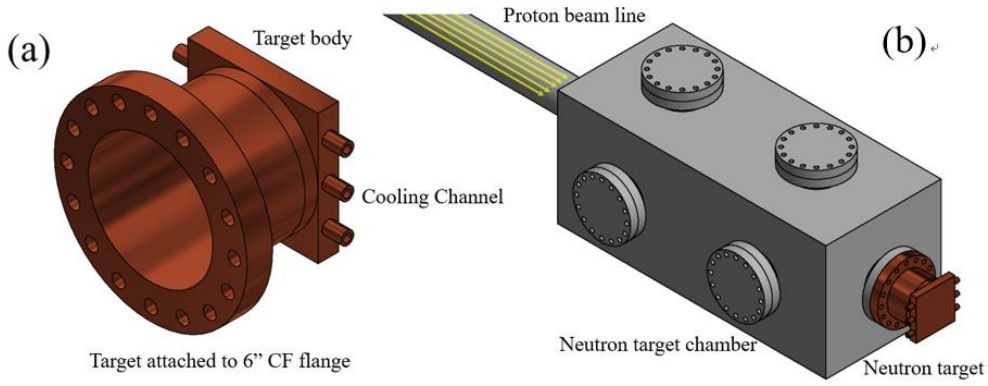

Figure 4.4. A drawing of target assembly and (b) installation to a beam current monitor chamber attached to the proton beam line.

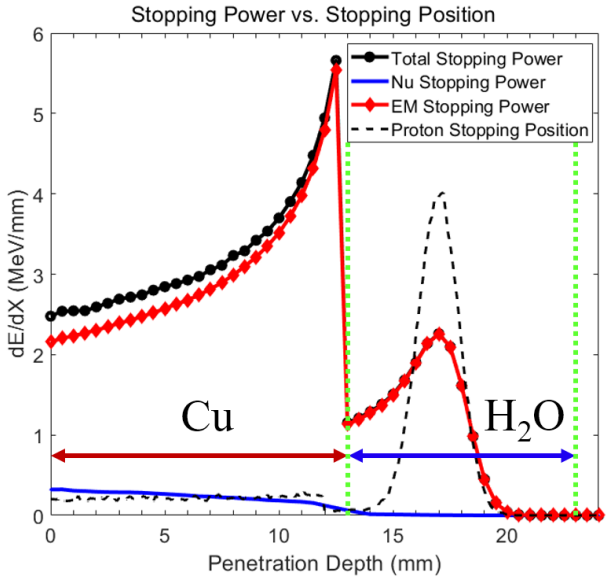

Figure 4.5. Stopping characteristics of 100-MeV proton beam impinging on the target assembly consisting of 13-mm thick Cu target body and 10-mm thick water cooling channel.

4.3. Thermal Analysis

Thermal analysis has been conducted with ANSYS Fluent simulation package [11] for the target assembly shown in Fig. 4.4(a). For a nominal operation of the 100-MeV proton accelerator, the beam diameter is and the average beam power deposited on the target assembly is assumed to be 30 mm and 2 kW, respectively. The power deposition profile along the beam propagation is the same as the stopping power profile shown in Fig. 4. Hence, it is used as a heat source profile in the thermal analysis using ANSYS Fluent code. Fig. 4.6(a) shows the dependence of the water flow rate from 0.3 Liter per minute (LPM) up to 7.5 LPM on the maximum temperature rise in the target assembly. The maximum temperature rise is found to be less than 40 K for the nominal flow rate of 7.5 LPM supplied by the utility. The temperature distribution on the target assembly is depicted in Fig. 4.6(b) for the flow rate of 7.5 LPM. It is clear that the surface irradiated by the proton beam is the hottest.

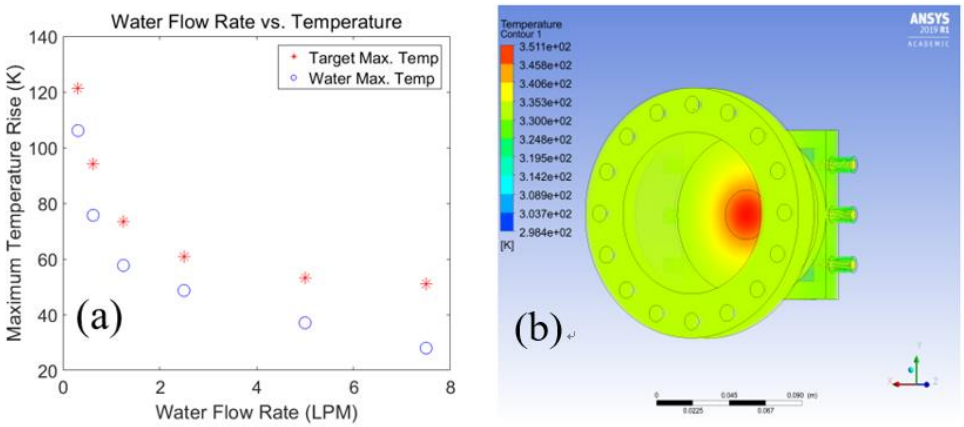

Figure 4.6. (a) The maximum temperature rise in the target assembly depending on the water flow rate and (b) the temperature distribution of the target assembly for the flow rate of 7.5 LPM.

4.4. Performance Evaluation

Neutron transport simulation with Geant4 has been conducted to evaluate the overall performance expected at the position which the irradiation station is located. As seen in Fig. 4.7, the concrete tunnel geometry as well as the position of target and irradiation station is implemented in the simulation to estimate the realistic neutron yield and spectrum at the irradiation station. Wall thickness is 2 m from all direction, and target and irradiation station is 5 m and 7 ° apart from each other.

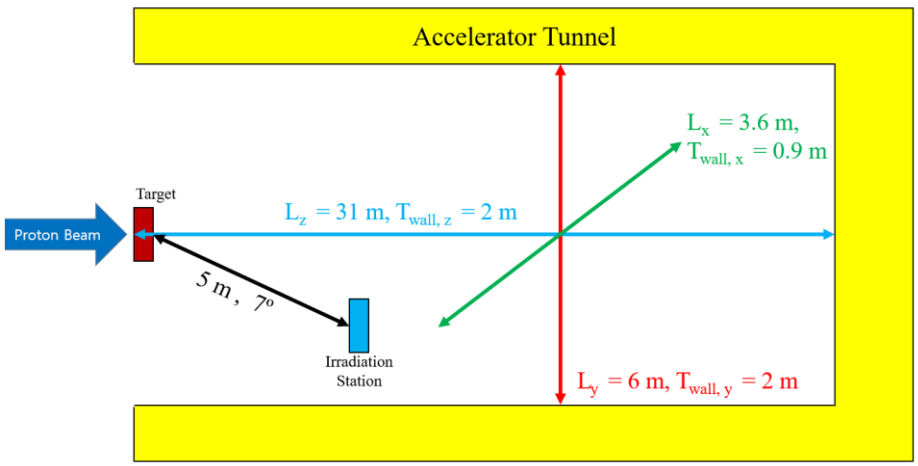

Figure 4.7. Target-irradiation station diagram implemented in simulation. Height, width, and length is indicated with x, y, and z axes respectively.

Performance of the target in perspective of soft error assessment is evaluated with the acceleration factor discussed earlier in chapter 1.2, the sum of the differential neutron energy spectrum divided by that of atmospheric neutron spectrum.

The simulation result estimates that the neutron yield at the irradiation station is 1.07×10^7 neutrons/cm^{2}s for the 100-MeV proton beam operating at the average power of 2 kW. The corresponding acceleration factor is calculated to be 2.24×10^9. The expected neutron spectrum at the irradiation station is compared with the atmospheric neutron spectrum multiplied by the acceleration factor in Fig. 4.8.

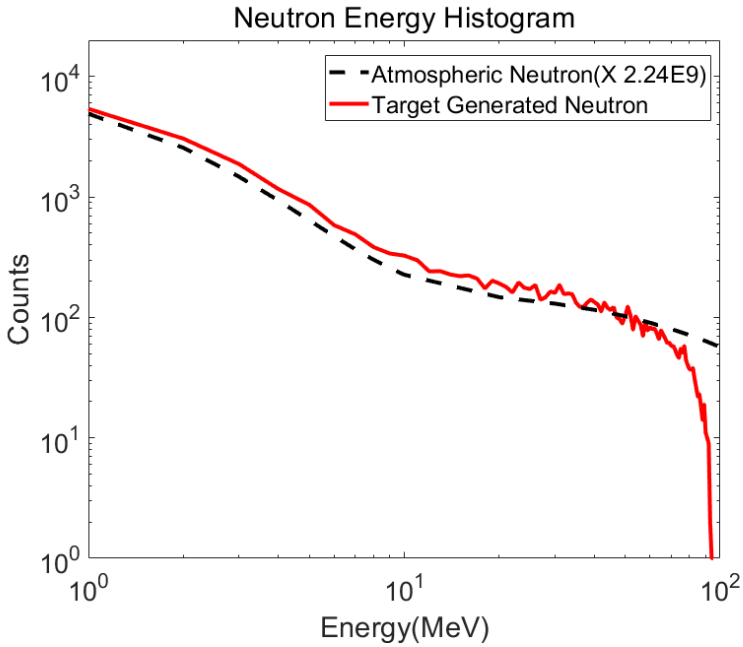

Figure 4.8. Comparison between the expected neutron spectrum at the irradiation station and the atmospheric neutron spectrum multiplied by the acceleration factor (2.24×10^9).

Chapter 5. Conclusion

The thesis encompasses a wide range of studies from fast neutron detection and assessment with simulation to design of a neutron target. Preliminary fast neutron generation with a Cu beam dump is conducted and verified with a preliminary neutron detection with a 1" stilbene scintillator coupled with a PMT. Presence of fast neutron is identified with PSD and its associated data processing, and neutron energy histogram is acquired by separating neutron signals from gamma signals. A simulation with Geant4 Monte-Carlo code is constructed with replicated geometry of experimental circumstances, with necessary physics models. The simulation encompasses the whole processes regarding the neutron generation, transport, and detector simulation so that simulation result can be directly compared with a minimal assumption for an estimation of neutron flux and neutron energy histogram. Simulation results shows a certain degree of agreement with experimental data which roughly verifies neutron yields and spectrum shape produced from the experiment.

Neutron TOF system is configured and tested with the fast neutrons. Gamma flash type TOF spectroscopy implemented in this measurement requires a proton beam pulse width as short as 20 ns to acquire a full energy spectrum with resolution of 10 % at 100 MeV. Nevertheless, verification of the TOF system is successfully accomplished by observing the maximum energy of neutrons generated by two different proton irradiation energies.

Furthermore, a new design for neutron target that is able to install on the beam line chamber is designed to produce neutrons appropriate for soft error testing of electronic devices. Cu is selected for the target material to produce the most atmospheric-like neutron spectrum, and other associated design in engineering aspect is conducted as well. Thermal design and analysis is carried to afford 2 kW of proton beam irradiation on target with 7.5 LPM water flow rate. Due to a matter of time, this research is described as unfinished for a full construction and for 100 MeV neutron source system, but following research will be accompanied in near future.

Bibliography

[1] M. S. Gordon, P. Goldhagen, K. P. Rodbell, T. H. Zabel, H. H. K. Tang, J. M. Clem, and P. Bailey, “Measurement of the Flux and Energy Spectrum of Cosmic-Ray Induced Neutrons on the Ground,” IEEE Trans. Nucl. Sci. 51(6), pp. 3427-3434, 2004.

[2] J. F. Ziegler, “Terrestrial cosmic rays,” IBM J. Res. Develop. 40(1), pp. 19-39, 1996.

[3] E. Normand, “Single event upset at ground level,” IEEE Trans. Nucl. Sci. 43(6), pp. 2742-2750, 1996.

[4] D. Lambert et al., “Analysis of quasi-monoenergetic neutron and proton SEU cross sections for terrestrial applications,” IEEE Trans. Nucl. Sci. 53(4), pp. 1890-1896, 2006.

[5] D. Lambert et al., “Neutron-induced SEU in SRAMs: Simulations with n-Si and n-O interactions,” IEEE Trans. Nucl. Sci. 52(6), pp. 2332-2339, 2005.

[6] J. Baggio, D. Lambert, V. Ferlet-Cavrois, P. Paillet, C. Marcandella, and O. Duhamel, “Single event upsets induced by 1–10 MeV neutrons in static-RAMs using mono-energetic sources,” IEEE Trans. Nucl. Sci. 54(6), pp. 2149-2155, 2007.

[7] H.H. Barschall et al., Neutron Sources For Basic Physics and Applications, Chapter 10, pp. 217 – 220, 1983.

[8] C. Andreani, A. Pietropaolo, A. Salsano, G. Gorini, M. Tardocchi, A. Paccagnella, S. Gerardin, C. D. Frost, S. Ansell, and S. P. Platt “Facility for fast neutron

irradiation tests of electronics at the ISIS spallation neutron source," Appl. Phys. Lett. 92, 114101, 2008.

[9] R. Baumann, The new JEDEC JESD89A test standard: how is it different than the old one and why should we use it?, RADECS 2007, Deauville, France, 2007.

[10] O.A. Shcherbakov et al., Characterization of The Neutron beam At The Radiation Resistance Test Facility In Catchina, the XXIII International Seminar on Interaction of Neutrons with Nuclei, 2015

[11] JEDEC Standard JESD89A, Oct. 2006. Available: http://www.jedec.org.

[12] Dario Bisello et al., "Neutron production targets for a new Single Event Effects facility at the 70 MeV Cyclotron of LNL-INFN," Physics Procedia 26, pp. 284-293, 2012.

[13] L. Saldana, N. Stemen. 'Pulse Shape Discrimination Methods', Yale University, July 2014.

[14] https://komac.kaeri.re.kr:448/komaceng/install/proton.do

[15] https://www.radiation-dosimetry.org/what-is-scintillation-counter-scintillation-detector-definition/

[16] Glenn F. Knoll, Radiation Detection and Measurement, Chapter 8, pp. 229 - 231.

[17] https://www.hamamatsu.com/us/en/product/type/R1924A/index.html

[18] https://hep.hamamatsu.com/eu/en/product/search/H11934-100/index.html

[19] https://www.caen.it/products/dt5751/

[20] https://www.caen.it/products/n6725/

[21] Y. Iwamoto, M. Fukuda, Y. Sakamoto, A. Tamii, K. Hatanaka, K. Takahisa, K. Nagayama, H. Asai, K. Sugimoto, and I. Nashiyama, “Evaluation of the white neutron beam spectrum for SEE testing at the RCNP cyclotron facility,” Nucl. Technol., vol. 173, pp. 210–217, 2011.

[22] A. Buffler, A.C. Comrie, F.D. Smit, H.J. Wörtche, Neutron spectroscopy with EJ299-33 plastic scintillator forEn=10–100 MeV, IEEE Trans. Nucl. Sci. 62 pp. 1422 , 2015.

[23] Rene Brun and Fons Rademakers, ROOT - An Object Oriented Data Analysis Framework, Proceedings AIHENP'96 Workshop, Lausanne, Sep. 1996, Nucl. Inst. & Meth. in Phys. Res. A 389 pp.81-86, 1997.

[24] MATLAB. version 9.3.0 (R2017b). Natick, Massachusetts: The MathWorks Inc, 2017.

[25] Allison, J.; Amako, K.; Apostolakis, J.; Araujo, H.; Arce Dubois, P.; Asai, M.; Barrand, G.; Capra, R.; Chauvie, S.; Chytracek, R.; Cirrone, G.A.P.; Cooperman, G.; Cosmo, G.; Cuttone, G.; Daquino, G.G.; et al. "Geant4 developments and applications" (PDF). IEEE Transactions on Nuclear Science, 2006.

[26] Geant4: Reference Physics List. https://geant4.web.cern.ch/node/628.

[27] G. Folger, V.N. Ivanchenko, J.P. Wellisch, “The binary cascade,” Eur. Phys. J. A21(3), pp. 407-417, 2004.

[28] A. V. Prokofiev, J. Blomgren, M. Majerle, R. Nolte, S. Rottger, S. P. Platt, C. X. Xiao, and A. N. Smirnov, “Characterization of the ANITA neutron Source for Accelerated SEE Testing at The Svedberg Laboratory,” in Proc. IEEE Radiation Effects Data Workshop, Quebec City, QC, Canada, pp. 166-173, 2009.

[29] http://lansce.lanl.gov/NS/instruments/ICEhouse/index.html.

[30] C. Andreani, A. Pietropaolo, A. Salsano, G. Gorini, M. Tardocchi, A. Paccagnella, S. Gerardin, C. D. Frost, S. Ansell, and S. P. Platt “Facility for fast neutron irradiation tests of electronics at the ISIS spallation neutron source,” Appl. Phys. Lett. 92, 114101, 2008.

[31] Gabriel J. DeSalvo and John A. Swanson. ANSYS Engineering Analysis System User's Manual. Houston, Pa.: Swanson Analysis Systems, 1985.

[32] Astrelin VT et al., “Blistering of the selected materials irradiated by intense 200 keV proton beam,” J. Nucl. Mater. 396, pp. 43-48, 2010.

[33] P. Lee, “Design of the 100 MeV proton-beam target system for the pulsed neutron source at the KOMAC,” J. Korean Phys. Soc. 73(8), pp. 1068-1072, 2018.

[34] Sang-Pil Yoon et al, “The Preliminary Design of the Neutron Production Target for the KOMAC Pulsed Neutron Source.” Transactions of the KOrean Nuclear Society Spring Meeting, 2017.

[35] Yaping Cheng et al., “The High-Speed After Pulse Measurement System for PMT.” Journal of Instrumentation, 2014.

[36] Seung Kyu Lee et al., “Scintillation Properties of Composite Stilbene Crystal for Neutron Detection,” Nuclear Science and Technology, Vol.1, pp.292-295, 2011.

Abstract in Korean

100 MeV 양성자 펄스 빔을 이용한 중성자 표적 시스템 개발 및 전산모사 연구

임 수 빈
에너지시스템공학부
(핵융합 및 플라즈마 공학 전공)
서울대학교 대학원

가속기 기반의 고속중성자원에 대한 수요는 시간이 지남에 따라 점점 더 증가하게 되었지만, 가속기 기반 중성자원에 대한 공급은 그에 비해 많지 않아 새로운 중성자원에 대한 개발의 중요성이 대두되었다. 본 연구에서는 특히 그중에서도 산업에서 가장 많은 수요가 있는 반도체 분야에서의 중성자원에 대한 연구를 수행하였으며, 그에 따라 가장 기초적인 섬광체 기반의 중성자 계측에서부터 Geant4 몬테칼로 코드를 이용한 중성자 생성에서부터 전달, 계측기 시뮬레이션에 이르기까지의 과정을 모사하여 단일 스틸벤 섬광체 기반 중성자 계측과의 결과와 비교하여 그 신뢰도를 검증하였다. 또한 해당 계측 결과를 기반으로 감마 플래시 타입 중성자 비행시간 측정 시스템을 구성하였으며, 해당 시스템을 이용하여 이후 양성자 단 펄스가 준비되었을 때 중성자 에너지 분포에 대한 정보를 확보할 수 있도록 준비하였다. 현 상황에서는 단 펄스가 준비되어있지 않아 해당 시스템을 이용해 해당 중성자의 에너지 분포 중 최고 에너지를 계측하였다.

현재는 구리 빔 덤프를 이용하여 중성자 생성을 수행하고 있지만, 이후 정식으로 중성자를 서비스하기 위한 중성자 표적의 개발도 수행하였다. 중성자 표적 물질 후보군 중 가장 대기중성자 스펙트럼과 유사한 구리를 이용하여 표적을 제작하였으며, 이에 따른 열적 디자인과 최대 2Kw 의 빔 파워에 대한 해석도 수행하였다. 따라서 결론적으로 중성자원을 안정적으로 제공하기 위한 기초적 연구 및 개발이 성공적으로 수행되었으며, 이는 근 미래에 양성자과학연구단에 새로이 설치될 가속기 기반 중성자원에 유용하게 쓰이게 될 수 있으리라 기대한다.

Keywords; 대기 중성자, 파쇄 중성자, 중성자 표적 설계, 중성자 계측, 방사선 계측, 섬광체 검출기, 몬테 칼로 방사선 해석

학 번: 2018-27834